

Temporal evolution of depolarization and magnetic field of FRB 20201124A

WAN-JIN LU,¹ ZHEN-YIN ZHAO,¹ F. Y. WANG,^{1,2,3} AND Z. G. DAI⁴

¹*School of Astronomy and Space Science, Nanjing University, Nanjing 210093, China*

²*Key Laboratory of Modern Astronomy and Astrophysics (Nanjing University), Ministry of Education, Nanjing 210093, China*

³*Purple Mountain Observatory, Chinese Academy of Sciences, Nanjing 210023, China*

⁴*Department of Astronomy, University of Science and Technology of China, Hefei 230026, China*

ABSTRACT

Fast radio bursts (FRBs) are energetic millisecond phenomena in radio band. Polarimetric studies of repeating FRBs indicate that many of these sources occupy extreme and complex magneto-ionized environments. Recently, a frequency-dependent depolarization has been discovered in several repeating FRBs. However, the temporal evolution of polarization properties is limited by the burst rate and observational cadence of telescopes. In this letter, the temporal evolution of depolarization in repeating FRB 20201124A is explored. Using the simultaneous variation of rotation measure and dispersion measure, we also measure the strength of a magnetic field parallel to the line-of-sight. The strength ranges from a few μG to $10^3 \mu\text{G}$. In addition, we find that the evolution of depolarization and magnetic field traces the evolution of rotation measure. Our result supports that the variation of depolarization, rotation measure and the magnetic field are determined by the same complex magneto-ionized screen surrounding the FRB source. The derived properties of the screen are consistent with the wind and the decretion disk of a massive star.

Keywords: Radio transient sources (2008); Magnetic fields (994); Interstellar medium (847)

1. INTRODUCTION

Fast radio bursts (FRBs) are energetic millisecond pulses in the radio band (Lorimer et al. 2007). They show diverse observational properties, including spectral morphology, energy distribution and polarization properties (Xiao et al. 2021; Zhang 2022; Petroff et al. 2022).

Recently, observations show that the polarization of FRBs has complex properties. The first repeating FRB source discovered, FRB 20121102A, is highly linear-polarized, while no circular component was found in L-band (Spitler et al. 2016; Hewitt et al. 2022). The ultra-large rotation measure ($\text{RM} \sim 10^5 \text{ rad m}^{-2}$, Michilli et al. 2018) implies the source is located in a complex and extreme magneto-ionic environment. The decreasing behavior of RM also favors a temporal variation scenario (Hilmarsson et al. 2021a; Feng et al. 2023a), i.e., an expanding ejecta (Margalit & Metzger 2018; Piro & Gaensler 2018; Zhao et al. 2021; Zhao & Wang 2021; Katz 2022; Yang et al. 2023). FRB 20201124A shows

significant temporal and frequency-dependent evolution of polarization properties (Xu et al. 2022). It is the first FRB showing RM reversal (Wang et al. 2022a). FRB 20190520B has been reported to be one of the weirdest repeating FRBs for its dramatic RM reversal and dispersion measure (DM) excess (Niu et al. 2022; Anna-Thomas et al. 2023). A magnetar/Be star binary model is proposed to explain the variations and reversal of RM of these two FRBs (Wang et al. 2022a), in which an FRB-generating magnetar orbits a Be-star companion with a “decretion” disk. In this model, RM variation is caused by the magnetized decretion disk. Importantly, a decretion disk with a toroidal magnetic field can naturally result in a sign change of RM. Subsequently, more repeating FRBs have shown RM variations (Mckinven et al. 2023a,b; Kumar et al. 2023), implying a dynamical magneto-ionic environment. However, FRB 20220912A shows a nearly zero local RM in two months, indicating a clean environment (Zhang et al. 2023; Feng et al. 2023b). Recently, a repeating FRB source FRB 20200120E discovered in M81 globular cluster also shows a modest RM according to the constraints on the Galactic halo contribution (Bhardwaj et al. 2021; Kirsten et al. 2022).

Since FRB 20201124A was discovered by the Canadian Hydrogen Intensity Mapping Experiment (CHIME) Collaboration (Chime/Frb Collaboration 2021), thousands of bursts were detected and well-measured during several active episodes (Xu et al. 2022; Zhou et al. 2022). Oscillation of both linear and circular polarization components is revealed from the large samples by sensitive monitoring campaign (Xu et al. 2022). Some bursts show depolarization that is concurrent with observed RM variation, which can be explained by differential Faraday rotation along different paths (Wang et al. 2022a). Feng et al. (2022) reported that five active repeating FRBs show frequency-dependent linear polarization fraction, which can be well described by RM scatter. The possible physical origin is the differential Faraday rotation along different paths (Beniamini et al. 2022; Yang et al. 2022). The frequency-dependent linear polarization is also studied in FRB 20180916B and some other repeating FRBs (Mckinven et al. 2023a,b). For RM-varying FRBs, the frequency-dependent linear polarization should be time-dependent, due to the changes of RM scatter. However, there is no evidence at present. In this Letter, we report the temporal evolution of depolarization in FRB 20201124A in a daily timescale for the first time. After the variations of RM and DM are determined, the strength of the magnetic field $|\langle B_{\parallel} \rangle|$ along the line of sight is also measured.

This Letter is organized as follows. We introduce the fitting procedure of the spectra in Section 2. The depolarization fit of burst samples and the temporal variation of the σ_{RM} and $|\langle B_{\parallel} \rangle|$ are given in Section 3. Discussion and conclusions are shown in Section 4.

2. SPECTRA FITTING

Active FRB repeaters allow us to measure the temporal evolution of the depolarization effect in a short timescale. However, not all of them have polarimetry measurements. Limited by the interchannel depolarization caused by the large rotation measure of FRBs and channel frequency of telescopes, repeaters like FRB 20121102A (Michilli et al. 2018) and FRB 20190520B (Anna-Thomas et al. 2023) are not suitable for the analysis. Therefore, we chose the repeating FRB 20201124A monitored by the Five-hundred-meter Aperture Spherical Telescope (FAST, Jiang et al. 2020). FRB 20201124A shows diverse observational properties, such as the oscillation of the degree of linear polarization (DoL) and temporal evolution of the RM (Xu et al. 2022; Jiang et al. 2022).

To measure the daily depolarization effect of active FRB repeaters, the DoL and central frequency need to be determined. Xu et al. (2022) obtained the DoL and

circular polarization component from the Stokes parameters. However, they only estimated the spectral width of each burst by performing the Gaussian fitting and taking the 3σ as the effective width owing to the unknown spectra shape of FRBs up-to-date. Some of the bursts are deviated from the Gaussian function. Therefore, they did not take the peak value of the Gaussian fitting result as the central frequency.

To fit the central frequency, we took the empirical assumption that the intrinsic spectra of FRBs could be fitted using a Gaussian function. Zhou et al. (2022) have also discovered a double-peak distribution of central frequency in the observations of FRB 20201124A after May 2021 based on the Gaussian fitting result. Firstly, we calculated the derivation δf_i from standard Gaussian spectra for the i -th bursts by fitting the Gaussian function

$$F(\nu) = F_0 + A \times \exp\left[-\frac{(\nu - f_c)^2}{2\sigma^2}\right], \quad (1)$$

where σ is the standard deviation and f_c is the central frequency. With the fitted result above as the initial parameters, we then performed a Markov Chain Monte Carlo (MCMC) fit using the Python package *emcee* (Foreman-Mackey et al. 2013) to obtain the more accurate result by iteration.

The spectral width W_{eff} is proportional to the fitted standard deviation σ . The mean value was the fitted central frequency f_c . There is also a latent double-peak Gaussian shape similar to the result of Zhou et al. (2022). We did not fit the two peaks of central frequency owing to the selection bias caused by those bursts whose f_c sits at the edge of FAST bandwidth. Therefore, not all the bursts with fitted spectra width and central frequency can be used to study the depolarization effect. Nevertheless, we determined a series of filter strategies as follows to obtain all the narrow-band samples.

1. Set the 3σ of the Gaussian function as the equivalent spectral half-width $W_{\text{eff}}/2$ and the FAST bandwidth is [1 GHz, 1.5 GHz]. The bursts should satisfy the following criteria: 1) The central frequency is located in the FAST bandwidth; 2) $W_{\text{eff}} > 40$ MHz and $W_{\text{eff}} < 600$ MHz; 3) The lower or upper 60% equivalent spectral width at least is covered by FAST bandwidth.
2. Considering the known radio frequency interference, the constraint on the FAST bandwidth is [1.05, 1.45] GHz. The bursts should satisfy the following criteria: 1) The central frequency is located in the FAST bandwidth; 2) The W_{eff} satisfies $20 \text{ MHz} < W_{\text{eff}} < 600 \text{ MHz}$;

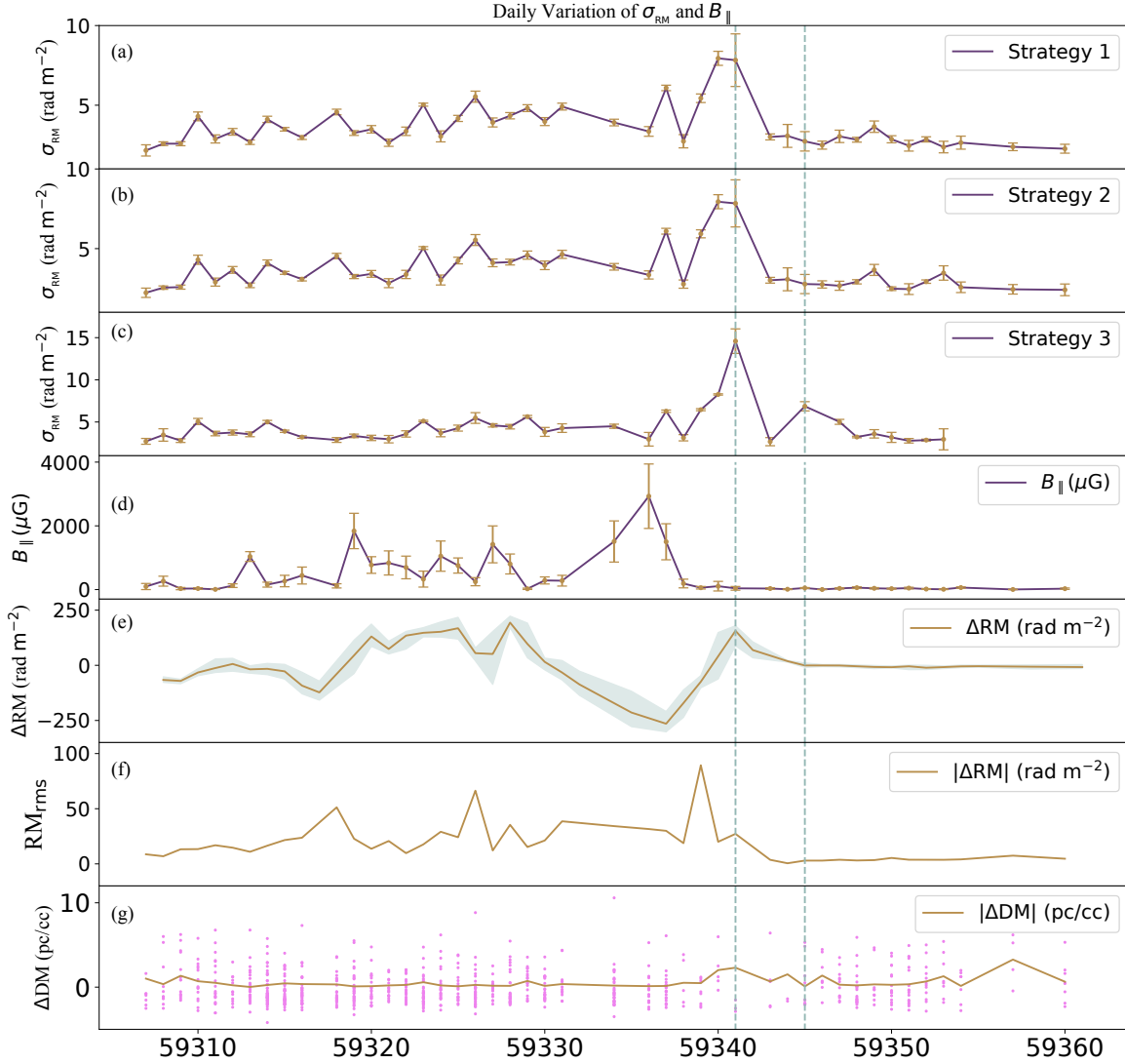


Figure 1. The temporal variation of σ_{RM} and $|B_{\parallel}|$ of FRB 20201124A in a daily timescale. The top three panels show σ_{RM} for the three strategies. The panel (d) shows the variation of B_{\parallel} . The panel (e) gives the RM variation $\Delta\text{RM}=\text{RM}_{\text{obs}}-\text{RM}_c$ and its range defined by the maximum and minimum of the daily RM (the light green region). RM_c is taken to be the average RM value within the active episode, which is $588.06 \text{ rad m}^{-2}$. The daily variation of the root-mean-square (rms) of RM is plotted in the panel (f). The daily variation and the scatter (violet dots) of the ΔDM is shown in the panel (g), similar with the definition of ΔRM . Two vertical dashed lines are used to show the simultaneous variation trend of σ_{RM} and ΔRM , which represent MJD = 59341 and 59345, respectively.

- 3) The lower or upper 85% equivalent spectral width at least is covered by FAST bandwidth;
 - 4) By artificial identification.
- The spectral width is defined the same as in Strategy 1.
3. Set the Full-Width-Half-Maximum (FWHM, i.e. $2\sqrt{2\ln 2}\sigma$) of the Gaussian function as the equivalent

spectral width W_{eff} and the FAST bandwidth is [1 GHz, 1.5 GHz]. Collecting the bursts whose W_{eff} is within the FAST bandwidth.

We collected 761, 808 and 399 bursts out of all 1863 bursts by applying these criteria, respectively. The next step is to fit the depolarization effect from daily bursts. We sorted the narrow-band bursts above by the barycen-

tric time of arrival at 1.5 GHz (Xu et al. 2022), from MJD = 59307 to 59360. The fitting function (Equation 2) from Burn (1966)

$$f_{\text{depol}} = 1 - \exp(-2\lambda^4\sigma_{\text{RM}}^2) \quad (2)$$

is used, where λ represents the wavelength of the electromagnetic wave in units of m and σ_{RM} is the standard deviation of the RM. This function assumes that the FRB source is 100% linearly polarized originally. For FRB 20201124A, it has been observed to show frequency-dependent polarization (Feng et al. 2022; Kumar et al. 2022; Hilmarsson et al. 2021b). Significant circular bursts were reported by Xu et al. (2022), which is considered to be generated by specific radiation mechanism (Wang et al. 2022b; Liu et al. 2023; Qu & Zhang 2023). We then excluded those highly circular polarized bursts from our filtered dataset. Therefore, Equation (2) is suitable for studying the temporal evolution of the depolarization effect of FRB 20201124A in L band.

We selected some of the daily depolarization fitting plots in Appendix (see Figure 3). Though the single-parameter exponential function poorly constrained for some data points, qualitative temporal variation could be distinguished.

Besides, RM is defined as

$$\text{RM} = 0.81 \text{ rad m}^{-2} \int \frac{(B_{\parallel}/\mu\text{G})n_e}{(1+z)^2} dl. \quad (3)$$

The average magnetic field parallel to the direction of line-of-sight $\langle B_{\parallel} \rangle$ could be extracted from the RM measurement. Furthermore, if the variation of both RM and DM are dominated by the same region (e.g. a plasma scattering screen), the absolute value of $\langle B_{\parallel} \rangle$ could be estimated as (Katz 2020)

$$|\langle B_{\parallel} \rangle| = 1.23 \frac{|\Delta\text{RM}|}{|\Delta\text{DM}|} \mu\text{G}. \quad (4)$$

The $|\Delta\text{RM}|$ and $|\Delta\text{DM}|$ represent the daily deviations from the average RM and DM value spanning this active episode, respectively. Equation (4) could be applied under the assumption that the variation of RM and DM are contributed by the same outer region of FRB source. The contribution of the Milky Way and Galactic halo maintains constant at a monthly timescale.

3. TEMPORAL VARIATIONS OF σ_{RM} AND $|\langle B_{\parallel} \rangle|$

The RM of the repeating FRB 20201124A has been reported to show significant irregular variation throughout the two-month observations performed by FAST (Xu et al. 2022). Similar to RM, we obtained the temporal variation of σ_{RM} with the 1σ uncertainty from

the daily depolarization fitting result introduced in Section 2. Figure 1 shows the temporal variation of the depolarization effect for three different selection strategies. The temporal variations for the three cases are similar, supporting that the selection strategy has little effect on the final result and the temporal evolution of σ_{RM} is physical. The σ_{RM} shows stochastic fluctuation at the early stage and significant amplification during the reversal of ΔRM . The evolution of σ_{RM} traces that of ΔRM , which supports they have the same origin. After the reversal, the variation is quenched, similar to the ΔRM .

Limited by the burst counts, several observations in the later stage could not perform the depolarization fit using strategy 3. The joint variation trend in Figure 1 shows that these polarimetric parameters are independent of different selection criteria on narrow-band bursts. Although some of the depolarization shows underfitting indicated by the p -value, the daily depolarization results are acceptable for two reasons: 1) The fitting function is a single-parameter quartic exponential function; 2) The majority unfitting data points were found before the significant enhancement of σ_{RM} (i.e. MJD = 59337) and they are clustered near the lower edge of bandwidth. The central frequency of these datapoints is lower than the fitted value because of the limited bandwidth of FAST. Thus, the actual σ_{RM} in these days should be lower than the current result, which would support the low and constant evolution at the early stage shown in Figure 1. We also test our method with the observational data from Feng et al. (2022), Mckinven et al. (2023a) and Mckinven et al. (2023b). The p -value of FRB 20190303A, FRB 20190417A and FRB 20180916B are comparable with the validated data points of ours. The low p -value may also be caused by other possibilities of depolarization, such as intrinsic property and internal depolarization (Mckinven et al. 2023a).

There are several data points misaligned with the RM variation, which could be caused by the limited burst counts within one day and unknown central frequency. Besides, the fluctuation of σ_{RM} and RM are quasi-simultaneous with each other. The variation of σ_{RM} traces the RM variation and supports the physical scenario that the magneto-ionized environment dominates the observational polarization properties of repeating FRB 20201124A, i.e., the depolarization and RM variation.

Taking the assumption that the variations of both RM and DM are contributed by the same region, we calculated the mean observed variation of the RM and DM from the daily data and figured out the variation of $|\langle B_{\parallel} \rangle|$ using equation (4) in the panel (d) of Figure 1.

Table 1. Fitting results of σ_{RM} and $|\langle B_{\parallel} \rangle|$

MJD	σ_{RM}	Counts/ χ^2/p	σ_{RM}	Counts/ χ^2/p	σ_{RM}	Counts/ χ^2/p	$ \langle B_{\parallel} \rangle $	$ \Delta\text{RM} $	$ \Delta\text{DM} $
	rad m ⁻²	-	rad m ⁻²	-	rad m ⁻²	-	μG	rad m ⁻²	cm ⁻³ pc
59307	2.2 ^{+0.4} _{-0.4}	8/2.95/0.004	2.2 ^{+0.3} _{-0.3}	6/1.72/0.054	2.7 ^{+0.3} _{-0.3}	4/1.41/0.125	95.96	78.76	1.01
59308	2.6 ^{+0.1} _{-0.1}	10/1.51/0.011	2.6 ^{+0.1} _{-0.1}	9/1.72/0.016	3.5 ^{+0.7} _{-0.7}	3/2.12/0.248	263.78	75.57	0.35
59309	2.6 ^{+0.1} _{-0.1}	18/1.47/0.002	2.6 ^{+0.1} _{-0.1}	17/1.06/0.002	2.8 ^{+0.2} _{-0.2}	11/2.10/0.062	30.61	33.55	1.35
59310	4.3 ^{+0.3} _{-0.3}	18/0.27/0.446	4.3 ^{+0.3} _{-0.3}	17/0.28/0.449	5.1 ^{+0.4} _{-0.4}	6/0.11/0.740	32.77	18.70	0.70
59311	2.9 ^{+0.3} _{-0.3}	22/1.47/<1e-3	2.9 ^{+0.3} _{-0.3}	22/1.42/<1e-3	3.6 ^{+0.3} _{-0.3}	10/1.01/0.073	6.91	2.87	0.51
59312	3.3 ^{+0.2} _{-0.2}	12/1.46/0.013	3.7 ^{+0.2} _{-0.2}	15/1.00/0.009	3.8 ^{+0.3} _{-0.3}	10/1.10/0.018	123.09	22.08	0.22
59313	2.7 ^{+0.1} _{-0.1}	39/2.03/<1e-3	2.7 ^{+0.1} _{-0.1}	35/1.91/<1e-3	3.5 ^{+0.3} _{-0.3}	13/0.62/0.026	1037.08	18.58	0.02
59314	4.1 ^{+0.2} _{-0.2}	41/1.26/0.022	4.1 ^{+0.2} _{-0.2}	44/1.23/0.016	5.0 ^{+0.2} _{-0.2}	25/1.12/0.398	154.85	32.10	0.26
59315	3.5 ^{+0.1} _{-0.1}	44/1.49/<1e-3	3.5 ^{+0.1} _{-0.1}	46/1.01/<1e-3	3.9 ^{+0.1} _{-0.1}	34/0.76/0.031	267.91	98.40	0.45
59316	3.0 ^{+0.1} _{-0.1}	30/2.14/<1e-3	3.1 ^{+0.1} _{-0.1}	36/1.90/<1e-3	3.2 ^{+0.1} _{-0.1}	14/2.76/0.009	440.80	130.89	0.37
59318	4.6 ^{+0.2} _{-0.2}	20/0.84/0.593	4.5 ^{+0.2} _{-0.2}	24/0.63/0.971	2.9 ^{+0.3} _{-0.3}	18/3.18/<1e-3	116.99	30.81	0.32
59319	3.3 ^{+0.1} _{-0.1}	28/2.07/<1e-3	3.2 ^{+0.1} _{-0.1}	32/2.12/<1e-3	3.4 ^{+0.2} _{-0.2}	11/3.16/0.009	1838.71	136.31	0.09
59320	3.5 ^{+0.2} _{-0.2}	20/1.97/<1e-3	3.4 ^{+0.2} _{-0.2}	21/2.00/<1e-3	3.1 ^{+0.3} _{-0.3}	11/2.55/0.006	770.62	71.77	0.11
59321	2.6 ^{+0.2} _{-0.2}	10/3.49/0.022	2.8 ^{+0.3} _{-0.3}	16/3.13/0.001	3.0 ^{+0.4} _{-0.4}	11/3.79/0.002	835.68	139.26	0.20
59322	3.4 ^{+0.3} _{-0.3}	27/2.29/<1e-3	3.4 ^{+0.3} _{-0.3}	27/2.23/<1e-3	3.6 ^{+0.4} _{-0.4}	17/2.63/0.001	694.04	148.46	0.26
59323	5.0 ^{+0.1} _{-0.1}	33/0.62/0.396	5.0 ^{+0.1} _{-0.1}	38/0.80/0.140	5.1 ^{+0.1} _{-0.1}	22/1.11/0.135	328.82	155.70	0.58
59324	3.0 ^{+0.3} _{-0.3}	19/3.75/<1e-3	3.0 ^{+0.3} _{-0.3}	19/3.67/0.001	3.7 ^{+0.4} _{-0.4}	13/2.88/0.007	1049.43	174.35	0.20
59325	4.2 ^{+0.2} _{-0.2}	17/1.18/0.010	4.3 ^{+0.2} _{-0.2}	19/1.08/0.006	4.3 ^{+0.4} _{-0.4}	13/1.51/0.013	754.52	61.12	0.10
59326	5.5 ^{+0.3} _{-0.3}	30/0.78/0.446	5.5 ^{+0.3} _{-0.3}	31/0.81/0.336	5.5 ^{+0.6} _{-0.6}	14/0.85/0.196	247.46	53.71	0.27
59327	3.9 ^{+0.3} _{-0.3}	19/1.36/0.001	4.1 ^{+0.2} _{-0.2}	20/1.10/0.001	4.6 ^{+0.2} _{-0.2}	10/1.04/0.011	1418.76	192.39	0.17
59328	4.3 ^{+0.2} _{-0.2}	24/0.69/0.035	4.2 ^{+0.2} _{-0.2}	29/0.85/0.002	4.4 ^{+0.3} _{-0.3}	18/1.06/<1e-3	803.20	99.27	0.15
59329	4.8 ^{+0.2} _{-0.2}	14/0.40/0.043	4.6 ^{+0.3} _{-0.3}	16/0.50/0.029	5.6 ^{+0.1} _{-0.1}	8/0.10/0.196	24.46	14.57	0.73
59330	4.0 ^{+0.2} _{-0.2}	24/3.15/0.004	4.0 ^{+0.3} _{-0.3}	21/1.32/0.001	3.8 ^{+0.5} _{-0.5}	9/2.39/0.009	286.44	34.96	0.15
59331	4.9 ^{+0.2} _{-0.2}	19/1.01/0.004	4.6 ^{+0.3} _{-0.3}	21/1.23/0.002	4.3 ^{+0.5} _{-0.5}	10/2.80/0.005	278.63	83.22	0.37
59334	3.9 ^{+0.2} _{-0.2}	33/1.74/<1e-3	3.9 ^{+0.2} _{-0.2}	32/1.74/<1e-3	4.5 ^{+0.2} _{-0.2}	17/1.79/0.004	1509.29	224.80	0.18
59336	3.4 ^{+0.3} _{-0.3}	15/2.05/0.002	3.3 ^{+0.3} _{-0.3}	15/1.71/0.004	3.0 ^{+0.8} _{-0.8}	3/7.01/0.321	2930.00	283.93	0.12
59337	6.1 ^{+0.2} _{-0.2}	26/0.88/0.350	6.1 ^{+0.2} _{-0.2}	23/1.00/0.719	6.3 ^{+0.1} _{-0.1}	16/1.00/0.402	1500.26	173.47	0.14
59338	2.7 ^{+0.4} _{-0.4}	2/0.32/0.616	2.8 ^{+0.3} _{-0.3}	3/0.15/0.502	3.1 ^{+0.4} _{-0.4}	2/0.11/0.787	190.27	79.77	0.52
59339	5.4 ^{+0.3} _{-0.3}	8/0.64/0.064	5.9 ^{+0.3} _{-0.3}	9/0.37/0.209	6.5 ^{+0.1} _{-0.1}	3/0.23/0.212	57.78	22.34	0.48
59340	7.9 ^{+0.4} _{-0.4}	6/0.41/0.113	7.9 ^{+0.4} _{-0.4}	6/0.41/0.113	8.3 ^{+0.1} _{-0.1}	3/0.04/0.214	106.37	174.60	2.02
59341	7.8 ^{+1.7} _{-1.7}	5/2.13/0.932	7.8 ^{+1.5} _{-1.5}	6/2.05/0.661	14.6 ^{+1.5} _{-1.5}	3/1.89/0.277	38.97	73.02	2.30
59343	3.0 ^{+0.2} _{-0.2}	6/1.58/0.164	3.0 ^{+0.2} _{-0.2}	7/1.81/0.074	2.7 ^{+0.5} _{-0.5}	3/6.48/0.203	32.78	17.98	0.67
59344	3.1 ^{+0.7} _{-0.7}	3/3.27/0.217	3.1 ^{+0.7} _{-0.7}	3/3.27/0.217	-	-	9.96	12.32	1.52
59345	2.7 ^{+0.6} _{-0.6}	6/4.66/0.031	2.8 ^{+0.6} _{-0.6}	6/3.62/0.060	6.9 ^{+0.5} _{-0.5}	2/0.10/0.811	49.13	3.44	0.09
59346	2.5 ^{+0.3} _{-0.3}	9/2.91/0.022	2.8 ^{+0.2} _{-0.2}	10/2.05/0.034	-	-	3.12	3.50	1.38
59347	3.0 ^{+0.4} _{-0.4}	11/0.88/0.157	2.7 ^{+0.3} _{-0.3}	16/1.21/0.006	5.0 ^{+0.3} _{-0.3}	6/0.20/0.539	36.66	8.61	0.29
59348	2.8 ^{+0.2} _{-0.2}	23/0.54/0.015	2.9 ^{+0.1} _{-0.1}	22/0.43/0.048	3.2 ^{+0.1} _{-0.1}	9/0.32/0.698	59.68	10.15	0.21
59349	3.7 ^{+0.4} _{-0.4}	10/0.88/0.062	3.7 ^{+0.3} _{-0.3}	11/1.28/0.033	3.6 ^{+0.5} _{-0.5}	7/1.80/0.089	39.92	10.63	0.33
59350	2.9 ^{+0.2} _{-0.2}	17/1.15/0.010	2.5 ^{+0.1} _{-0.1}	17/1.69/0.002	3.2 ^{+0.6} _{-0.6}	3/1.07/0.475	29.00	6.53	0.28
59351	2.5 ^{+0.3} _{-0.3}	15/2.60/0.027	2.5 ^{+0.3} _{-0.3}	15/2.60/0.027	2.8 ^{+0.3} _{-0.3}	7/3.30/0.206	46.49	12.78	0.34
59352	2.9 ^{+0.2} _{-0.2}	14/0.28/0.015	2.9 ^{+0.1} _{-0.1}	15/0.27/0.014	2.9 ^{+0.1} _{-0.1}	8/0.13/0.504	16.63	9.15	0.68
59353	2.4 ^{+0.4} _{-0.4}	5/1.85/0.040	3.5 ^{+0.5} _{-0.5}	7/0.69/0.079	2.9 ^{+1.2} _{-1.2}	2/3.84/0.566	9.58	10.08	1.29
59354	2.7 ^{+0.4} _{-0.4}	3/0.48/0.297	2.6 ^{+0.3} _{-0.3}	6/1.75/0.199	-	-	62.84	7.41	0.15
59357	2.4 ^{+0.2} _{-0.2}	4/0.32/0.288	2.4 ^{+0.3} _{-0.3}	5/0.64/0.072	-	-	3.85	10.24	3.27

NOTE—Column 2-3, 4-5, 6-7 are the fitting results, reduced χ^2 and p -value by adopting filter strategies 1, 2 and 3 as introduced in Section 2. Column 8-10 are the line-of-sight magnetic field, $|\Delta\text{RM}|$ and $|\Delta\text{DM}|$ by applying Equation 4. Failed fitting of several datasets are caused by limited burst counts.

Similar to the $|\Delta\text{RM}|$ introduced in Figure 1, the $|\Delta\text{DM}|$ was obtained from the daily deviation of the FAST dataset by maximizing the coherent power of bursts (see Xu et al. (2022) and references therein). The strength of magnetic field is from a few μG to $10^3 \mu\text{G}$, as shown in Figure 1. The variation of $|\langle B_{\parallel} \rangle|$ spans three orders of strength and quickly decreases to nearly zero as the RM is back to a constant, which is also tracked by the variation of the root-mean-square of daily RM (panel (f) in Figure 1). We estimated the uncertainty of $|\langle B_{\parallel} \rangle|$, which could be mainly caused by the small variation of ΔDM . Mild variation of ΔDM with comparable measurement precision would lead to dramatic enhancement of $|\langle B_{\parallel} \rangle|$. The small variation of ΔDM is supported by at least the two following observations. Firstly, the detection of FRB 20201124A requires that the optical depth of free-free absorption should be smaller than unity, which constrains the value of ΔDM is less than unity (see eq.(3) of (Xu et al. 2022)). Secondly, some bursts of this FRB show the characteristic of Faraday conversion (Xu et al. 2022). As discussed by Wang et al. (2022a) and Xu et al. (2022), a large magnetic field is required for Faraday conversion. Because the value of ΔRM is about a few hundred rad m^{-2} , large magnetic fields require small ΔDM . The error bars in the panel (f) of Figure 1 describe a temporal evolution trend qualitatively.

The result suggests an active and turbulent environment that either the value of the magnetic field or the direction is changing. For example, the toroidal configuration in a rotating disk or stellar wind could explain the changing direction of the magnetic field (Wang et al. 2022a; Zhao et al. 2023). We also compare the value of $|\langle B_{\parallel} \rangle|$ of other FRBs. Lin & Dai (2016) proposed that the average magnetic field strengths of FRBs along the line of sight can be derived from the absolute value of RM and DM. Wang et al. (2020) derived $|\langle B_{\parallel} \rangle|$ of FRBs by adopting a strong assumption that RM and DM are from the same medium. The mean value $1.77 \mu\text{G}$ is found, which is significantly lower than our results. The dataset applied in Wang et al. (2020) only contained a few active FRB repeaters, while the knowledge of Faraday active medium around the FRB source was remarkably expanded at the dawn of 2020s. Recently, CHIME reported a series of systematic polarimetry measurements of FRB repeaters (Mckinven et al. 2023b). The line-of-sight magnetic field is comparable with our result ($10^1 - 10^3 \mu\text{G}$). A large value of 3-17 mG is derived for FRB 20121102A (Katz 2020).

4. DISCUSSION AND CONCLUSIONS

The significant variation of σ_{RM} and $|\langle B_{\parallel} \rangle|$ traces the temporal evolution of the local magnetized environment

of FRB 20201124A within one active episode. We updated this daily σ_{RM} fitting result in the $|\text{RM}| - \sigma_{\text{RM}}$ relation in Feng et al. (2022). The σ_{RM} variation is consistent with the 1σ uncertainty, as introduced in Figure 2. The daily RM- σ_{RM} points from this work actually overweight the FRB 20201124A to provide an inappropriate linear fit for different FRB repeaters. The scatter of these data points simply shows the variation of FRB 20201124A and is consistent within the 1σ uncertainty of Feng et al. (2022).

A binary model containing a massive Be star and a magnetar has been applied to explain the stochastic variation of RM and the reversal of the magnetic field (Wang et al. 2022a). The azimuthal magnetic field distribution in the decretion disk of the Be star provides insight into the RM and magnetic reversal of repeating FRBs such as FRB 20201124A and FRB 20190520B. Different physical scenarios such as stellar wind and disk have been discussed theoretically (Zhao et al. 2023). The temporal variation of σ_{RM} could constrain different models by applying the depolarization effect caused by multi-path propagation through the plasma screen.

The frequency-dependent relation of linear polarization has been reported and studied in detail among radio pulsars and extragalactic radio sources (Burn 1966; Gardner & Whiteoak 1966). Yang et al. (2022) estimated the value of σ_{RM} contributed by the screen as

$$\sigma_{\text{RM}} = 0.81 \text{ rad m}^{-2} \left(\frac{\sqrt{l_s \Delta R}}{1 \text{ pc}} \right) \left(\frac{\delta(n_e B_{\parallel})_{l_s}}{1 \text{ cm}^{-3} \mu\text{G}} \right). \quad (5)$$

The thickness ΔR and the transverse separation from the line-of-sight l_s varies from different models. $\left(\frac{\delta(n_e B_{\parallel})_{l_s}}{1 \text{ cm}^{-3} \mu\text{G}} \right)$ represents the fluctuation of electron density and the magnetic field along the line-of-sight. We compared the contribution of stellar wind and disk, respectively. For the stellar decretion disk model, we adopted the formula of electron density from Section 2.1 in Zhao et al. (2023) and assumed the radius at which the electron density maintains half of the value at the stellar surface to be the critical size $r_{d,0.5}$. For the stellar wind model, we defined the critical size as mentioned in the disk model.

Assuming that the stellar mass M_* and radius R_* to be $8M_{\odot}$ and $5R_{\odot}$ respectively, we estimated the transverse separation from the line-of-sight l_s when σ_{RM} varies from 2 to $\sim 8 \text{ rad m}^{-2}$. Taking the $\left(\frac{\delta(n_e B_{\parallel})_{l_s}}{1 \text{ cm}^{-3} \mu\text{G}} \right) \sim 10^8 \text{ cm}^{-3} \mu\text{G}$ (Wang et al. 2022a), the transparent separation l_s in disk model rises from 1.2×10^{10} to $2 \times 10^{11} \text{ cm}$. The variation in stellar wind model is 1.2×10^{10} to $1.9 \times 10^{11} \text{ cm}$. The result is also comparable with the

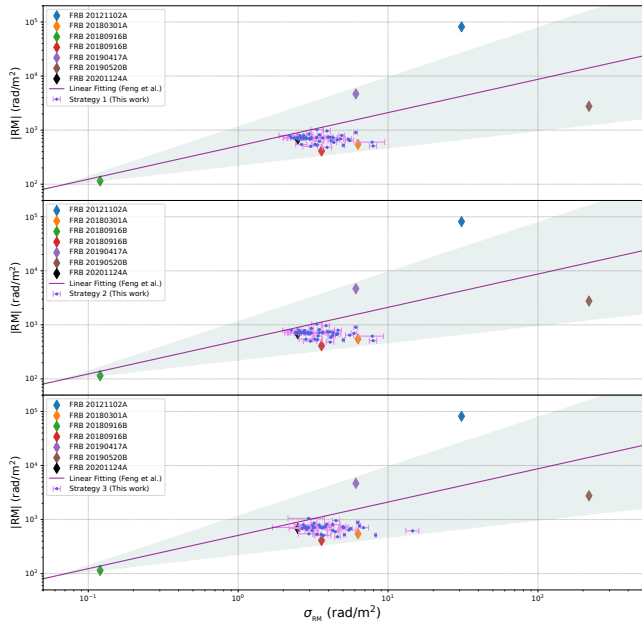


Figure 2. The $|RM|$ - σ_{RM} relation. Blue dots with 1σ errorbar are the daily result of FRB 20201124A in this work. The red line is the updated fitting linear function with 1σ uncertainty and the purple line is from Feng et al. (2022) with larger uncertainty.

geometric estimation in Zhao et al. (2023) and inhomogeneous clumps.

The fluctuation of electron density implies that the massive star in a binary system could originally produce the scattering screen, although these two models are still difficult to distinguish from the temporal variation of σ_{RM} . For Be stars, they both contribute to the temporal variations of RM and σ_{RM} . The periastron passage of the magnetar can corrupt the structure of the screen dynamically through the spin-down luminosity and tidal forces (Reig 2011; Wang et al. 2022a). The stellar wind would recover before the next passage (i.e. in one orbital period) due to its high velocity 3000 km/s

(Snow 1981). While the radial velocity of the decretion disk is much less than the sound speed (Okazaki 2001). The Galactic Be binary system PSR B1259-63/LS 2883 has shown significant differences between the DM and RM of the pulsed emission from one periastron to the next (Johnston et al. 2005). These differences indicate that the local properties of the Be star disk encountered by the pulsar, such as the disk density and magnetic field, change considerably between periastron passages (Johnston et al. 2005). The possible reason is the inhomogeneity of the disk caused by the spin-down luminosity and tidal forces of the pulsar. Monitoring campaigns in these passage stages may reveal more details in the future and give it a chance to apply in repeating FRBs.

In summary, we have investigated the temporal evolution of depolarization and magnetic field parallel to the line-of-sight in repeating FRBs for the first time. The strength of a magnetic field is from a few to $10^3 \mu\text{G}$. The evolution of depolarization and magnetic field traces the evolution of rotation measure, which supports that the variation of depolarization, rotation measure and the magnetic field are determined by the same complex magneto-ionized screen surrounding the FRB source. In the binary scenario, the derived properties of the screen can put constraints on the wind and the decretion disk of massive stars.

ACKNOWLEDGEMENTS

We thank the anonymous referee for helpful comments that were helpful in improving the manuscript. This work was supported by the National Natural Science Foundation of China (grant Nos. 12273009 and 11833003), the National SKA Program of China (grant Nos. 2022SKA0130100 and 2020SKA0120300), and the China Manned Space Project (CMS-CSST-2021-A12). This work made use of data from FAST, a Chinese national mega-science facility built and operated by the National Astronomical Observatories, Chinese Academy of Sciences.

REFERENCES

- Anna-Thomas, R., Connor, L., Dai, S., et al. 2023, *Science*, 380, 599, doi: [10.1126/science.abo6526](https://doi.org/10.1126/science.abo6526)
- Beniamini, P., Kumar, P., & Narayan, R. 2022, *MNRAS*, 510, 4654, doi: [10.1093/mnras/stab3730](https://doi.org/10.1093/mnras/stab3730)
- Bhardwaj, M., Gaensler, B. M., Kaspi, V. M., et al. 2021, *ApJL*, 910, L18, doi: [10.3847/2041-8213/abeaa6](https://doi.org/10.3847/2041-8213/abeaa6)
- Burn, B. J. 1966, *Monthly Notices of the Royal Astronomical Society*, 133, 67, doi: [10.1093/mnras/133.1.67](https://doi.org/10.1093/mnras/133.1.67)
- Chime/Frb Collabortion. 2021, *The Astronomer’s Telegram*, 14497, 1
- Feng, Y., Li, D., Yang, Y.-P., et al. 2022, *Science*, 375, 1266, doi: [10.1126/science.abl7759](https://doi.org/10.1126/science.abl7759)
- Feng, Y., Jiang, J., Zhou, D., et al. 2023a, *The Astronomer’s Telegram*, 15980, 1
- Feng, Y., Li, D., Zhang, Y.-K., et al. 2023b, arXiv e-prints, arXiv:2304.14671, doi: [10.48550/arXiv.2304.14671](https://doi.org/10.48550/arXiv.2304.14671)

- Foreman-Mackey, D., Hogg, D. W., Lang, D., & Goodman, J. 2013, *Publications of the Astronomical Society of the Pacific*, 125, 306, doi: [10.1086/670067](https://doi.org/10.1086/670067)
- Gardner, F. F., & Whiteoak, J. B. 1966, *Annual Review of Astronomy and Astrophysics*, 4, 245, doi: [10.1146/annurev.aa.04.090166.001333](https://doi.org/10.1146/annurev.aa.04.090166.001333)
- Hewitt, D. M., Snelders, M. P., Hessels, J. W. T., et al. 2022, *MNRAS*, 515, 3577, doi: [10.1093/mnras/stac1960](https://doi.org/10.1093/mnras/stac1960)
- Hilmarsson, G. H., Spitler, L. G., Main, R. A., & Li, D. Z. 2021a, *MNRAS*, 508, 5354, doi: [10.1093/mnras/stab2936](https://doi.org/10.1093/mnras/stab2936)
- . 2021b, *MNRAS*, 508, 5354, doi: [10.1093/mnras/stab2936](https://doi.org/10.1093/mnras/stab2936)
- Jiang, J.-C., Wang, W.-Y., Xu, H., et al. 2022, *Research in Astronomy and Astrophysics*, 22, 124003, doi: [10.1088/1674-4527/ac98f6](https://doi.org/10.1088/1674-4527/ac98f6)
- Jiang, P., Tang, N.-Y., Hou, L.-G., et al. 2020, *Research in Astronomy and Astrophysics*, 20, 064, doi: [10.1088/1674-4527/20/5/64](https://doi.org/10.1088/1674-4527/20/5/64)
- Johnston, S., Ball, L., Wang, N., & Manchester, R. N. 2005, *MNRAS*, 358, 1069, doi: [10.1111/j.1365-2966.2005.08854.x](https://doi.org/10.1111/j.1365-2966.2005.08854.x)
- Katz, J. I. 2020, *Monthly Notices of the Royal Astronomical Society: Letters*, 501, L76, doi: [10.1093/mnrasl/slaa202](https://doi.org/10.1093/mnrasl/slaa202)
- Katz, J. I. 2022, *MNRAS*, 510, L42, doi: [10.1093/mnrasl/slab128](https://doi.org/10.1093/mnrasl/slab128)
- Kirsten, F., Marcote, B., Nimmo, K., et al. 2022, *Nature*, 602, 585, doi: [10.1038/s41586-021-04354-w](https://doi.org/10.1038/s41586-021-04354-w)
- Kumar, P., Shannon, R. M., Lower, M. E., et al. 2022, *Monthly Notices of the Royal Astronomical Society*, 512, 3400, doi: [10.1093/mnras/stac683](https://doi.org/10.1093/mnras/stac683)
- Kumar, P., Luo, R., Price, D. C., et al. 2023, arXiv e-prints, arXiv:2304.01763, doi: [10.48550/arXiv.2304.01763](https://doi.org/10.48550/arXiv.2304.01763)
- Lin, W.-L., & Dai, Z.-G. 2016, *Research in Astronomy and Astrophysics*, 16, 38, doi: [10.1088/1674-4527/16/3/038](https://doi.org/10.1088/1674-4527/16/3/038)
- Liu, Z.-N., Wang, W.-Y., Yang, Y.-P., & Dai, Z.-G. 2023, *ApJ*, 943, 47, doi: [10.3847/1538-4357/acac23](https://doi.org/10.3847/1538-4357/acac23)
- Lorimer, D. R., Bailes, M., McLaughlin, M. A., Narkevic, D. J., & Crawford, F. 2007, *Science*, 318, 777, doi: [10.1126/science.1147532](https://doi.org/10.1126/science.1147532)
- Margalit, B., & Metzger, B. D. 2018, *ApJL*, 868, L4, doi: [10.3847/2041-8213/aaedad](https://doi.org/10.3847/2041-8213/aaedad)
- Mckinven, R., Gaensler, B. M., Michilli, D., et al. 2023a, *ApJ*, 950, 12, doi: [10.3847/1538-4357/acc65f](https://doi.org/10.3847/1538-4357/acc65f)
- . 2023b, arXiv e-prints, arXiv:2302.08386, doi: [10.48550/arXiv.2302.08386](https://doi.org/10.48550/arXiv.2302.08386)
- Michilli, D., Seymour, A., Hessels, J. W. T., et al. 2018, *Nature*, 553, 182, doi: [10.1038/nature25149](https://doi.org/10.1038/nature25149)
- Niu, C. H., Aggarwal, K., Li, D., et al. 2022, *Nature*, 606, 873, doi: [10.1038/s41586-022-04755-5](https://doi.org/10.1038/s41586-022-04755-5)
- Okazaki, A. T. 2001, *PASJ*, 53, 119, doi: [10.1093/pasj/53.1.119](https://doi.org/10.1093/pasj/53.1.119)
- Petroff, E., Hessels, J. W. T., & Lorimer, D. R. 2022, *Astronomy and Astrophysics Review*, 30, 2, doi: [10.1007/s00159-022-00139-w](https://doi.org/10.1007/s00159-022-00139-w)
- Piro, A. L., & Gaensler, B. M. 2018, *ApJ*, 861, 150, doi: [10.3847/1538-4357/aac9bc](https://doi.org/10.3847/1538-4357/aac9bc)
- Qu, Y., & Zhang, B. 2023, *MNRAS*, 522, 2448, doi: [10.1093/mnras/stad1072](https://doi.org/10.1093/mnras/stad1072)
- Reig, P. 2011, *Ap&SS*, 332, 1, doi: [10.1007/s10509-010-0575-8](https://doi.org/10.1007/s10509-010-0575-8)
- Snow, T. P., J. 1981, *ApJ*, 251, 139, doi: [10.1086/159448](https://doi.org/10.1086/159448)
- Spitler, L. G., Scholz, P., Hessels, J. W. T., et al. 2016, *Nature*, 531, 202, doi: [10.1038/nature17168](https://doi.org/10.1038/nature17168)
- Wang, F. Y., Zhang, G. Q., Dai, Z. G., & Cheng, K. S. 2022a, *Nature Communications*, 13, 4382, doi: [10.1038/s41467-022-31923-y](https://doi.org/10.1038/s41467-022-31923-y)
- Wang, W.-Y., Jiang, J.-C., Lee, K., Xu, R., & Zhang, B. 2022b, *MNRAS*, 517, 5080, doi: [10.1093/mnras/stac3070](https://doi.org/10.1093/mnras/stac3070)
- Wang, W.-Y., Zhang, B., Chen, X., & Xu, R. 2020, *MNRAS*, 499, 355, doi: [10.1093/mnras/staa2693](https://doi.org/10.1093/mnras/staa2693)
- Xiao, D., Wang, F., & Dai, Z. 2021, *Science China Physics, Mechanics, and Astronomy*, 64, 249501, doi: [10.1007/s11433-020-1661-7](https://doi.org/10.1007/s11433-020-1661-7)
- Xu, H., Niu, J. R., Chen, P., et al. 2022, *Nature*, 609, 685, doi: [10.1038/s41586-022-05071-8](https://doi.org/10.1038/s41586-022-05071-8)
- Yang, Y.-P., Lu, W., Feng, Y., Zhang, B., & Li, D. 2022, *The Astrophysical Journal Letters*, 928, L16, doi: [10.3847/2041-8213/ac5f46](https://doi.org/10.3847/2041-8213/ac5f46)
- Yang, Y.-P., Xu, S., & Zhang, B. 2023, *MNRAS*, 520, 2039, doi: [10.1093/mnras/stad168](https://doi.org/10.1093/mnras/stad168)
- Zhang, B. 2022, arXiv e-prints, arXiv:2212.03972, doi: [10.48550/arXiv.2212.03972](https://doi.org/10.48550/arXiv.2212.03972)
- Zhang, Y.-K., Li, D., Zhang, B., et al. 2023, arXiv e-prints, arXiv:2304.14665, doi: [10.48550/arXiv.2304.14665](https://doi.org/10.48550/arXiv.2304.14665)
- Zhao, Z. Y., & Wang, F. Y. 2021, *ApJL*, 923, L17, doi: [10.3847/2041-8213/ac3f2f](https://doi.org/10.3847/2041-8213/ac3f2f)
- Zhao, Z. Y., Zhang, G. Q., Wang, F. Y., & Dai, Z. G. 2023, *Astrophysical Journal*, 942, 102, doi: [10.3847/1538-4357/aca66b](https://doi.org/10.3847/1538-4357/aca66b)
- Zhao, Z. Y., Zhang, G. Q., Wang, F. Y., Tu, Z.-L., & Wang, F. Y. 2021, *ApJ*, 907, 111, doi: [10.3847/1538-4357/abd321](https://doi.org/10.3847/1538-4357/abd321)
- Zhou, D. J., Han, J. L., Zhang, B., et al. 2022, *Research in Astronomy and Astrophysics*, 22, 124001, doi: [10.1088/1674-4527/ac98f8](https://doi.org/10.1088/1674-4527/ac98f8)

5. APPENDIX

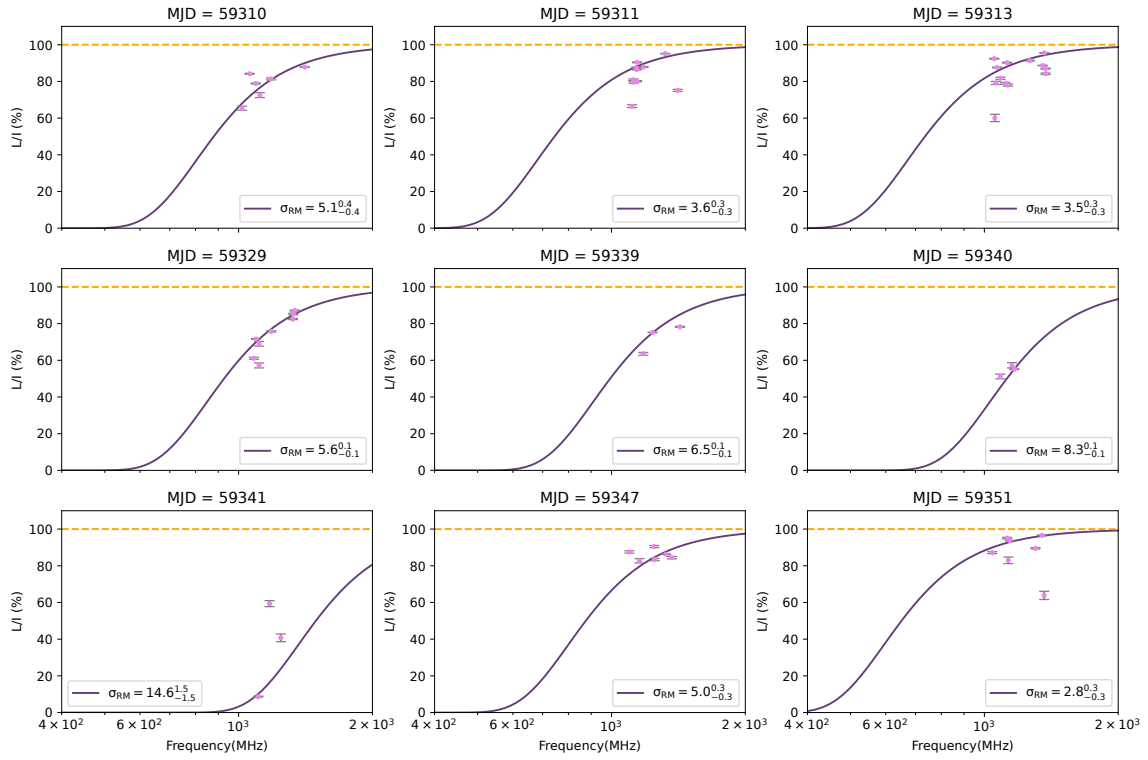


Figure 3. The exemplified daily depolarization fitting plots filtered by strategy 3 (see Section 2). Orange dashed lines represent the 100% degree of linear polarization. Purple curves show the depolarization fitting results of selected data points (magenta) with error bars.